Available online at www.sciencedirect.com
SCIENCE DIRECT®
Polymer 44 (2003) 3279–3289
polymer
www.elsevier.com/locate/polymer

Nanoscale molecular cavity in crystalline polymer membranes studied by molecular dynamics simulation

Yoshinori Tamai[a,*], Mitsuhiro Fukuda[b]

[a]*Department of Applied Physics, Faculty of Engineering, Fukui University, Fukui 910-8507, Japan*
[b]*Textile Materials Science Laboratory, Hyogo University of Teacher Education, Yashiro, Hyogo 673-1494, Japan*

Received 14 January 2003; received in revised form 24 February 2003; accepted 28 February 2003

Abstract

The size, shape, and connectivity of cavities in the crystals of syndiotactic polystyrene were investigated by molecular dynamics simulation. Cluster analysis of the free volume in the crystals clearly reveals the cavity structures: large individual holes are in an orderly manner connected by narrow channels. We call such a cavity structure a 'molecular cavity'. The diffusion behavior and solubility of gases in the molecular cavity were also simulated. The extremely high solubility of a larger gas and the controllable diffusion path in the narrow channels proved the applicability of the concept of the molecular cavity to high performance separation membranes.

Keywords: Polystyrene; Crystal; Free volume

1. Introduction

The concept of a 'molecular cavity' is represented by a nanoscale cavity with regular size, regular shape, and ordered connectivity [1]. The schematic representations of the molecular cavity are shown in Fig. 1. Various types of cavity structures can be designed according to the combination of the cavity size, shape, and connectivity. Separation membranes with controlled molecular cavities are expected to have a significantly high permselectivity. The cavity size is large enough for a particular molecule to permeate; the regularity of the cavity structure certifies the precise separation. The concept of the molecular cavity will provide a breakthrough in the precise separation of substances, impacting the technological fields of great urgency: the environment, energy, and pharmaceuticals. The concept alters the common knowledge that polymer crystals are virtually impermeable to gas transport.

Various clathrate compounds, in which guest molecules are hosted in the crystalline cages, are widely known [2–4]. The emptied forms of these compounds, if they exist, may be candidates for the molecular cavity. Most of the emptied forms are, however, unstable; the cages are broken. Zeolites [5], nanoporous mineral materials, are exceptional ones with stable empty cage structures (though they are thermodynamically in a metastable state). It is quite challenging to develop organic polymer materials which have precisely controlled molecular cavities.

Syndiotactic polystyrene (s-PS) is known for its unusual crystal polymorphism [6,7]. There are four main polymorphs for s-PS: α, β, γ, and δ forms. The α [8–11] and β [12,13] forms have the all *trans* (*TTTT*) conformation. The δ form is a clathrate compound with various guests, e.g. toluene [14], iodine [15], and 1,2-dichloroethane [16]. The emptied δ_e form [17] can be obtained by the extraction of solvent molecules from the δ form. The δ_e form is rather stable below 400 K and transformed into the γ form at higher temperature [6,17–20]. The main-chain conformation of the δ, δ_e, and γ forms is s(2/1)2 helical (*TTGG*). The stability of the δ_e form and the structural phase transition from the δ_e to γ forms were studied by MD simulation in our previous study [21].

The atomic coordinate data, which were determined by an X-ray diffraction experiment, suggested the presence of nanopores in the δ_e form [17]. The sorption behavior of chloroform [22], 1,2-dichloroethane [23], and carbon dioxide [24] supports the presence of the nanopores in the δ_e form. The conformational selectivity of 1,2-dichloroethane, favoring the *trans* conformers over *gauche* ones,

* Corresponding author. Tel./fax: +81-776-27-8032.
E-mail address: tamai@polymer.apphy.fukui-u.ac.jp (Y. Tamai).

0032-3861/03/$ - see front matter © 2003 Elsevier Science Ltd. All rights reserved.
doi:10.1016/S0032-3861(03)00214-3

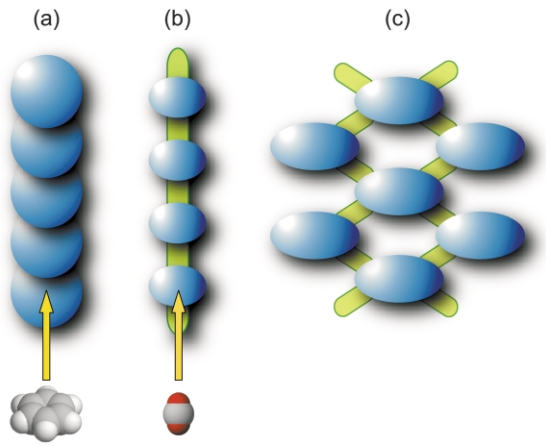

Fig. 1. Examples of schematic representation of the 'molecular cavity': (a) large cavities are directly connected, so as to form a tube, (b) small cavities are connected by narrow channels, like a capillary, (c) three-dimensional array of large cavities, which are connected by narrow channels. Particular size substances can be permeate through the tube (a) and capillary (b). Substances with particular shape and size can be preferentially absorbed into the controlled molecular cavities (c).

was examined by sorption experiments in combination with the conformational analysis of the guest in the cavity [25]. For this behavior, the semicrystalline material based on s-PS δ form was denoted as 'thermoplastic molecular sieves' by Guerra et al. [25]. The preferential complexing of *p*-xylene from mixed solvents of *m*- and *p*-xylene was also reported [26]. These experiments imply the existence of the molecular cavities which have significant selectivity for particular substances.

The quantitative analysis of the size, shape, and connectivity of cavities is essential to understand the permeation mechanism of substances in the crystals. Although the size distribution of cavities can be estimated by several experimental techniques such as the positronium annihilation spectroscopy, it is much difficult to directly observe the shape of the individual cavities and the connectivity between them. A molecular dynamics (MD) simulation, in combination with the free volume analysis, is a powerful tool to directly determine those properties [27–34]. Moreover, the cavity structures can be directly related to the diffusion and sorption behavior, which can also be investigated by a molecular simulation [32,33].

The molecular transport in liquids and glasses, the glass transition phenomena, and the diffusion coefficients of small penetrants in polymers have been correlated with the free volume [35–40]. In those investigations, there are several definitions of the free volume and in some case it is treated as a kind of adjustable parameter. A more rigorous theoretical method for determining the free volume was developed based on the atomistic MD simulation since late 1980s. Shah et al. calculated the free volumes in the polymer microstructures of polypropylene (PP) and poly-(vinyl chloride) (PVC), which are available to penetrant molecules of different sizes, by using a Monte Carlo method [27]. Rigby and Roe evaluated the distribution of occupied and unoccupied space in the systems of alkane-like chain molecules using both the Voronoi tessellation and the hard probe method [28]. The Delaunay tessellation method was applied for PP and bisphenol-A polycarbonate (PC) by Arizzi et al. [29]. The connectivity of the free volume was also analyzed by means of a cluster analysis; the volume distribution and the shape of individual free volume clusters were evaluated. The cluster analysis has also been performed for the other systems, e.g. PP [30], polybutadienes (PBD) [31], and poly(dimethyl siloxane) (PDMS) [32,33]. The channel structures were related to the diffusion behavior of small penetrants in polymers. A 'phantom bubble' method was also proposed by Lee and Mattice and was applied to polyethylene (PE) [34]. All those calculations have been applied for amorphous polymer systems.

In the crystalline polymers which have molecular cavity, the free volume is also closely related to the permeation of small penetrants. Milano et al. [41] evaluated the shape and volume of cavities in the δ_e form crystal by a numerical procedure. In their calculation, no thermal motions were included; the cavity volumes were evaluated for fixed crystal structures, which were determined by the X-ray diffraction experiments. The thermal fluctuation of the cavity structure is much important for the solution and diffusion of small penetrants in the crystal because the permeation occurs as a consequence of the cooperative motion between the penetrants and the polymer matrix. The connectivity of the cavities is not presented in their paper. Milano et al. [42] also investigated the diffusion behavior of He and CO_2 in the δ_e form by the MD simulation. In their simulation, however, the monoclinic crystal cell was translated into a quasi-orthorhombic MD unit cell for a technical requirement. This procedure affected the shape and edge lengths of the crystal unit cell; the length of the *a*- and *b*-axes were 5% smaller and 6% larger, respectively, than the experimental values [42]. Such marked deviations of the cell dimensions may affect significantly the anisotropy of diffusivity of small penetrants in the crystal because the narrow channels are sensitive to the crystal structure. Therefore, a more improved simulation study is needed to the quantitative understanding of the cavity structure. A comparison of the cavity structures between the δ_e form and the other polymorphs is also of much interest.

In this study, an extensive molecular dynamics (MD) simulation has been performed for the several polymorphs of s-PS, the α, β, δ, and δ_e forms. All the degrees of freedom of the unit cell, i.e. the three edge lengths and the three angles between them, are allowed to fluctuate, by using the triclinic periodic boundary condition. The longer cut off length of 14 Å was used in combination with the larger systems which contain approximately 10,000 atoms. The size, shape, and connectivity of the cavities in the crystal are analyzed by the free volume analysis. The connectivity of individual cavities is evaluated by a cluster analysis for the free volume. The concept of the molecular cavity is developed based on the various cavity structures in the

different polymorphs of s-PS. The characteristics of the cavity structures are also confirmed by the diffusion behavior of noble gases in the crystals, based on the long-time runs of MD simulation. The solubilities of several gases are also calculated by a molecular simulation method. The peculiar behavior of the diffusion and solubility of gases in the molecular cavity is related to the cavity structures.

2. Simulation details

2.1. Model

The polymorphs studied in this paper are listed in Table 1, associated with the total numbers of atoms and crystal units in an MD unit cell. As for the δ form, the complex with toluene, δ_{Tl}, and that with *p*-xylene, $\delta_{p\,X}$, were simulated. The initial structures were generated from the crystal structures determined by X-ray diffraction experiments [10,13,14,17]. The total numbers of atoms were 9216–12,288, depending on the crystal forms. The three-dimensional periodic boundary condition was applied. The crystals were modeled as single crystals in which an infinite number of monomer units is connected along the *c*-axis.

The potential model and the procedure for the MD simulation are the same as those used in the previous study [21]. The bonded interactions of the bond angle, torsion angle, and improper torsion angle, and the nonbonded Lennard-Jones and Coulomb interactions were included in the potential function. Bond lengths were constrained by the SHAKE method [43]. The nonbonded potential parameters are listed in Table 2. The potential parameters of s-PS were taken from the all-atom force field, AMBER [44]. The partial charges of s-PS were assigned, following the ab initio calculation of Smith et al. [45]. The potential parameters of the gases are taken from the literature [46–48]. The long-range nonbonded interactions were smoothly cut off at 14 Å on the basis of the distances between the centers of mass of neutral monomer units. The contribution of the Coulomb part to the total nonbonded potential energy is less than 5% in this system; therefore, the application of the cutoff method to the Coulomb potential does not affect the MD trajectories. The contributions to the pressure and the potential energy from the long tail of the Lennard-Jones potential were also included [49]. Because the radial distribution function does not converge on unity in the short distance for the crystals which contain large cavities, the cut off length affects the density and potential energy, and especially the *b*-axial spacing of the porous δ_e form. Therefore, the cut off length should be as long as possible. We confirmed that the cut off length of 14 Å is enough for the convergence of these properties.

Table 1
Crystal structures of s-PS and number of crystal units and atoms, N_{unit} and N_{atom}, respectively, in a MD unit cell

Crystal	Space group	Conformation	N_{unit}	N_{atom}
α[a]	*P*3	*TTTT*	2 × 2 × 8	9216
β[b]	$P2_12_12_1$	*TTTT*	6 × 2 × 8	12,288
δ_{Tl}[c]	$P2_1/a$	$(TTGG)_2$	3 × 4 × 6	11,376
$\delta_{p\,X}$[d]	$P2_1/a$	$(TTGG)_2$	3 × 4 × 6	11,808
δ_e[e]	$P2_1/a$	$(TTGG)_2$	3 × 4 × 6	9216

[a] Ordered modification α″ [10].
[b] Ordered modification β″ [13].
[c] Clathrate compound with toluene [14].
[d] Clathrate compound with *p*-xylene [14].
[e] Emptied clathrate form [17].

Table 2
Nonbonded potential parameters

Type	σ (Å)	ε (kJ/mol)	*q* (*e*)	Comment
CT	3.400	0.4580	0.0	Aliphatic C [44,45]
CA[a]	3.400	0.3601	−0.085	Aromatic C [44,45]
CA[b]	3.400	0.3601	0.0	Aromatic C [44,45]
HC	2.650	0.0657	0.0	Aliphatic H [44,45]
HA	2.600	0.0628	+0.085	Aromatic H [44,45]
HE	2.280	0.0850	0.0	He [46]
NE	2.720	0.3906	0.0	Ne [46]
AR	3.410	0.9960	0.0	Ar [46]
Cc	2.785	0.2412	+0.596	C of CO_2 [47]
Oc	3.014	0.6908	−0.298	O of CO_2 [47]
OO	3.090	0.3710	0.0	O of O_2 [48]
NN	3.310	0.3102	0.0	N of N_2 [48]

Combination rules for unlike atoms are $\sigma_{ij} = (\sigma_{ii} + \sigma_{jj})/2$ and $\varepsilon_{ij} = \sqrt{\varepsilon_{ii}\varepsilon_{jj}}$.
[a] Bonded to aromatic hydrogen, HA.
[b] Bonded to aliphatic carbon, CT.

2.2. Molecular dynamics simulation

The temperature and pressure tensors were controlled by the Nosé [50] and Parrinello–Rahman [51] methods; both the size and shape of the unit cell were allowed to fluctuate. The equations of motion were solved by a variant of the Verlet algorithm [52,53] with a time step of 1 fs, which is sufficiently short for the conservation of the Hamiltonian. The Verlet neighbor list [49] was used with automatically updating the list by monitoring the displacements of atoms. The oscillation periods of the MD cell dimensions, τ_h, were carefully calibrated by adjusting the virtual mass for the cell vectors W_h [50]. The choice of $W_h = 1 \times 10^4$ amu produced the τ_h value of approximately 3–10 ps, except for the *c*-axis. The time corresponds to one that sound travels in an MD unit cell (the longitudinal and transversal sound velocities in PS are 2400 and 1150 m/s, respectively). The τ_h value of the *c*-axis was shorter because of the connectivity of the chains. The virtual mass for the time scaling parameter, W_s, was practically set to 5×10^6 amu Å^2, which produced the oscillation period of $\tau_s \sim 5$ ps. To increase the efficiency of equilibration, W_s was set to 2×10^5 amu Å^2 ($\tau_s \sim 1$ ps) for the initial equilibration run of 10 ps.

MD simulations were performed at 300 K under ambient

pressure for 150 ps for each sample; the trajectories during the last 100 ps were used for the free volume analysis. The temperature was then increased to 350, 400, 450, and 500 K. The equilibration run of 20 ps, followed by the sampling run of 100 ps, was performed at each temperature. Although the δ_e form is transformed into the γ form above 400 K in the laboratory experiments, the structure of the δ_e form is held up to 500 K in our model, as presented in the previous study [21]. The superheated state could easily be obtained in the simulation because of the restriction of the unit cell and the infinite connectivity of the main-chains. Simulations under the experimentally inaccessible condition are also meaningful to understand the diffusion mechanism. Therefore, the simulation was also performed at up to 500 K. In order to simulate the diffusion behavior of gases in the s-PS polymorphs, the long-time runs of up to 5 ns was performed at each temperature after inserting 20 gas molecules into the separate cavities. The simulation runs were separately performed for three gas species, helium (He), neon (Ne), and argon (Ar).

A cluster machine with 28 Intel processors was used for the simulation along with the molecular simulation program PAMPS [32] coded and developed by one of the authors (Y.T.).

2.3. Free volume analysis

The free volume analysis was performed by a method similar to one described elsewhere [27,31–33,54,55]. In this method, the free volume is defined as the region into which a spherical probe can be inserted without overlapping to the host matrix atoms. A brief description of the method is given below. Each atom was modeled as a hard sphere with a radius of $\sigma/2$, i.e. the van der Waals radius, where σ is the Lennard-Jones size parameter shown in Table 2. The unit cell was divided into triclinic grid points with an interval of approximately 0.2 Å. The total number of grid points in an MD unit cell amounts to approximately 2×10^7. The minimum distance from each grid point to the nearest hard-sphere surface, R_m, was calculated. The R_m value represents the radius of the largest hard-sphere that could be inserted at the grid point in question. If the grid point resides within the hard spheres, R_m becomes a negative value. The lower limit of R_m is equal to $-\sigma_{max}/2$, i.e. -1.70 Å in the present system, where σ_{max} is the Lennard-Jones size parameter of the largest host-matrix atoms. The physical meaning of negative R value was also described by Pohorille and Pratt [54,55] in their study on the cavity distributions in molecular liquids. The probability density of R_m, $P_m(R_m)$, was then calculated, evaluating the R_m values for all the grid points. The insertion probability $P(R)$ was calculated as

$$P(R) = \int_R^\infty P_m(R')\mathrm{d}R' \tag{1}$$

The physical meaning of $P(R)$ is the fraction of volumes which are accessible for a probe of radius R. The continuous distribution of $P(R)$ can be obtained by this method. The distribution of $P(R)$ was averaged over 20 configurations for each crystal.

The connectivity of accessible volume (ACV) was investigated by a cluster analysis. Each grid point in ACV has up to six bonds with neighboring sites. Two neighboring grid points belong to the same cluster if both are accessible to a probe of radius R. The analysis was performed for 53 probes with R ranging from 0 to 2 Å for each crystal. The properties of the individual cavities were averaged, weighted by the cluster volume, as

$$\langle A \rangle_V = \frac{\sum V_i A_i}{\sum V_i}, \tag{2}$$

where A_i is one of the properties and V_i is the volume of ith ACV cluster. Note that the definition of the average cluster volume, $\langle V \rangle_V$, is different from the cavity volume calculated by Milano et al. [41]. The former means the average volume which can be accessible for the center of the probe, while the latter means the volume of the overlapping region with the probes ($R = 1.8$ Å), which are located on the accessible grid points.

2.4. Solubility

The chemical potentials of the gases were calculated by the particle insertion method [33,56]. The excluded volume map sampling (EVMS) [57] was used to raise the efficiency of sampling. The excluded volume map was constructed by dividing the MD unit cell into triclinic grid points with an interval of approximately 0.2 Å. 100,000 insertion trials of test molecules were attempted only for the nonexcluded volume of the configuration. The samplings were averaged over 20 configurations. The excess chemical potential μ_r was calculated as

$$\mu_r = -kT \ln\left[\frac{\langle WV \exp(-\psi/kT)\rangle_N}{\langle V \rangle_N}\right] \tag{3}$$

where ψ is the potential energy of the inserted (ghost) molecule with the surrounding real molecules, W is the weight of EVMS, which is equal to the nonexcluded volume fraction, V is the volume of the unit cell, and $\langle \ldots \rangle_N$ denotes the ensemble average over N molecules of the host matrix [33,56–58]. The solubility was estimated by

$$S = \exp(-\mu_r/kT) \tag{4}$$

3. Results and discussion

3.1. Crystal structures

The densities and the crystal cell dimensions obtained from the simulation are listed in Table 3, compared with the experiments. All the crystal structures were stable during

Table 3
Density and crystal cell dimensions of s-PS polymorphs

Crystal	ρ (g/cm^3)	a (Å)	b (Å)	c (Å)	γ (°)
Simulation					
α	1.054	25.82	26.26	5.03	119.9
β	1.091	8.79	28.61	5.04	90.0
δ_{TI}	1.091	17.47	13.42	7.79	122.0
$\delta_{p\,X}$	1.112	17.62	13.30	7.86	122.0
δ_e	0.959	17.38	11.73	7.81	115.0
Experiment[a]					
α	1.034	26.26	26.26	5.04	120
β	1.08	8.81	28.82	5.06	90
δ_{TI}	1.11	17.58	13.26	7.71	121.2
δ_e	0.977	17.4	11.85	7.70	117

[a] References are listed in the footnote of Table 1.

the simulation runs. The experimental values were satisfactorily reproduced by the simulation. Therefore, the application of the present model to the simulation of s-PS crystals is justified. The removal of solvents from the clathrate δ form results in the shrinkage of the *b*-axis by approximately 10%, accompanying the reduction of the angle γ. Generally speaking, the densities of the crystalline polymers are 10–15% higher than those of the amorphous phase. The densities of the α and β forms are, however, not so different from that of amorphous s-PS, 1.055 g/cm^3. The density of the δ_e form is, furthermore, markedly lower than that of amorphous s-PS, in spite of shrinkage along the *b*-axis. Such a peculiar behavior has not been reported for other polymers except for crystalline poly(4-methyl-1-pentene), whose density is comparable with that of the amorphous phase [59]. The markedly low density of the δ_e form implies the existence of large cavities in the crystal.

The structure of the $\delta_{p\,X}$ form is almost the same as that of the δ_{TI} form. This is consistent with the experiment: the structure of the δ_{TI} form is defined such that one of two methyl groups of each *p*-xylene molecule is randomly eliminated [13]. In this study, the $\delta_{p\,X}$ form is used as a reference of the closely packed δ form.

3.2. Free volume analysis

The projections of the static free volume, i.e. the volumes which are not occupied by any atoms, are shown in Fig. 2. The regions were calculated as the ACV for a probe of $R = 0$. The visualization of the ACV permits easy classification of the cavity structures. Large cavities are clearly observed in the δ_e form. These cavities construct a nanoscale three-dimensional array. On the other hand, the regular cavities in the β form are too narrow for penetrants to occupy or to pass through. Therefore, the system is not considered to have molecular cavities, as in the case of ordinary polymer crystals. Cavities parallel to the *c*-axis are seen in the α form.

Fig. 3 shows the insertion probability $P(R)$, the fraction of volumes accessible for a probe of radius R. Note that the thermal fluctuation of the crystal structure is taken into account in our calculation. The small portions of large holes, which are spontaneously formed in the polymer matrix, significantly affect the sorption and diffusion behavior of small penetrants in the polymers [32,33]. Therefore, the same functions as in Fig. 3 are plotted by using the semi-logarithmic scale in Fig. 4, in order to emphasize the low probability regions. The values at the intersection, $P(0)$, which represent the static free volume fraction, are listed in Table 4. The small value of $P(0)$ (0.267) and narrow distribution of $P(R)$ for the $\delta_{p\,X}$ form imply a closely packed clathrate form. In the δ_e form, $P(0)$ is large (0.381) and the distributions of $P(R)$ are markedly broad; there are large cavities into which penetrants with a radius larger than 2 Å can be inserted. Because the size and shape of cavities vary with the motion of the polymer chains, a large hole of 2.2 Å radius is occasionally observed in the δ_e form.

Fig. 5 shows the volume-weighted average of the individual cluster volume, $\langle V(R)\rangle_V$, as a function of the probe radius R. For a probe of $R = 0$, most of the grid points belong to the largest cluster, which is continuously spread over the entire system. With increasing radius R, ACVs are divided into many small clusters. The cluster volume decreases critically at a particular probe radius. The critical probe radius, R_c, approximated from the point of inflection, reflects the radius of channels between cavities. The values of R_c are listed in Table 4. Not only the δ_e but also the α form has a large R_c. The channel size is, however, somewhat smaller than the cavity size in the δ_e form, ~2 Å in radius. The volume-weighted cavity volume distributions, $P_V(V)$, which were calculated for a probe of radius 1 Å, are shown in Fig. 6. The average cluster volumes, $\langle V(1)\rangle_V$, are also listed in Table 4. Only the δ_e form has the distinct large cavities. The cavity volume of the δ_e form fluctuates around the average value, 28.92 Å^3, ranging from 10 to 50 Å, as a consequence of the thermal motion of the polymer matrix. This suggests the importance of molecular motion even in the single crystals.

Images of the ACV cluster for the probe of the critical radius R_c are shown in Fig. 7, associated with the skeletons of the polymer chains. Note that only one representative continuous cluster is shown for each crystal form; many other clusters like this exist in the system. The connectivity of the clusters varies with time. In the δ_e form, the large flat cavities of full length ~1 nm are stacked in the *c*-axial direction. This hypothesis is consistent with the NMR

Table 4
Free volume, $P(0)$, critical probe radius, R_c, and average cluster volume for a probe of 1 Å, $\langle V(1)\rangle_V$

Crystal	$P(0)$	R_c (Å)	$\langle V(1)\rangle_V$ (Å^3)
α	0.321	0.70	4.76
β	0.297	0.46	1.42
$\delta_{p\,X}$	0.267	0.42	0.22
δ_e	0.381	0.60	28.92

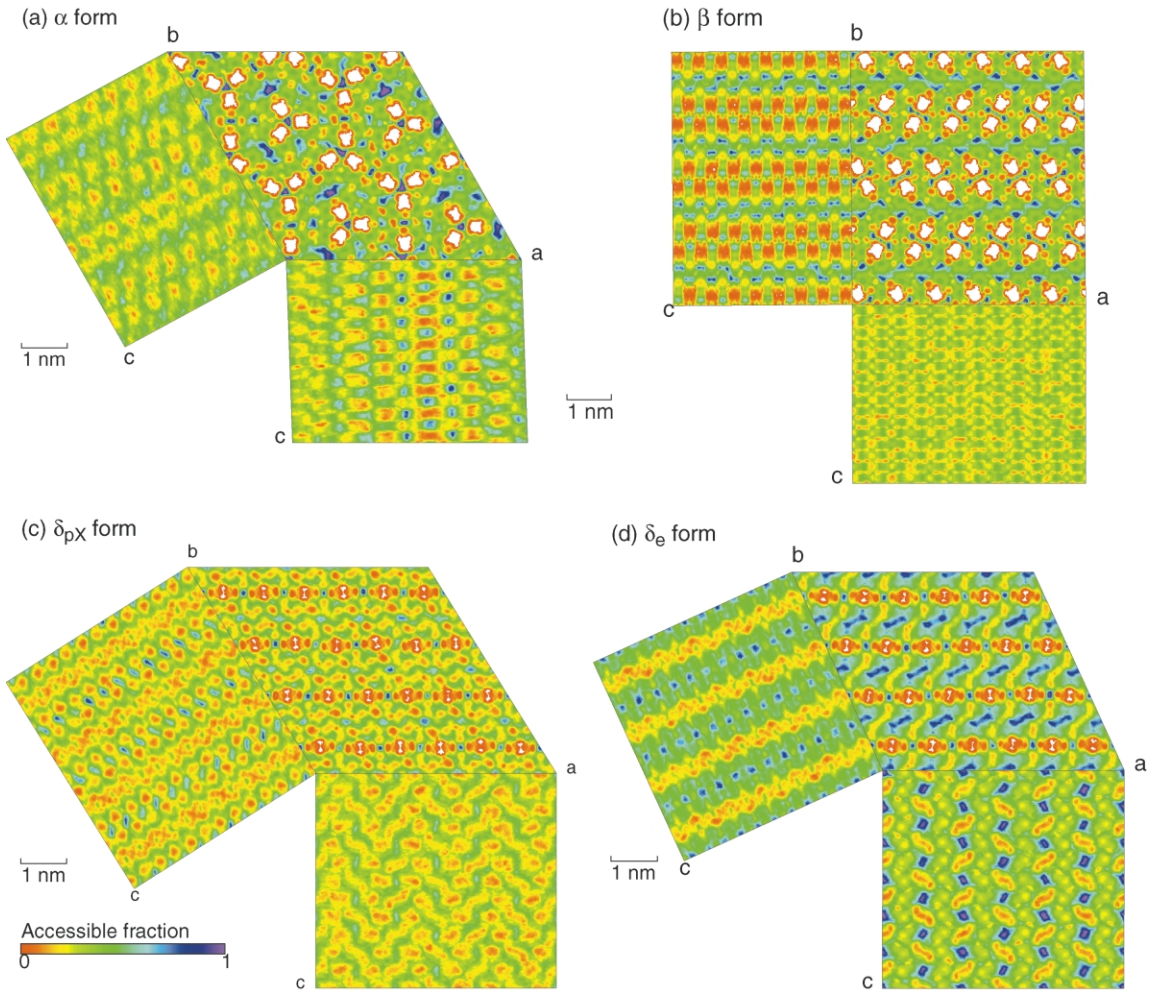

Fig. 2. The ACV for a probe of radius $R = 0$ (i.e. static free volume), calculated for the final configuration of the sampling runs. MD unit cells are projected onto $a-b$, $b-c$, and $c-a$ planes. The accessible fraction means the fraction of accessible grid points for the direction normal to the paper. The violet regions are vacancies while the red regions are occupied by atoms. The white regions are out of the ACV, i.e. the perfectly occupied (inaccessible) regions.

measurements of benzene and toluene in the δ form [60]; benzene rotates about the C_6 symmetry axis on a plane, while toluene does not. The methyl groups of toluene are fitted into the bay of cavities which are seen in the $a-b$ plane in Fig. 7(b). The shape of *p*-xylene is just fitted in that of the cavity. This supports the preferential complexing of *p*-xylene from mixed solvents of *m*- and *p*-xylene [26]. The cavities in the α form are connected continuously in straight lines along the *c*-axis, though the cavity size is not so large (∼1.5 Å).

The cavity in the δ_e form can appropriately be called a 'molecular cavity' because it satisfies the criteria of (1) nanoscale size, (2) regular shape, and (3) ordered connectivity. The considerably large individual holes are connected by narrow channels, as schematically represented by type (c) in Fig. 1. In contrast, the cavity structure in the α form has a somewhat different character: the narrow channels are aligned in one direction. The cavity constructs a molecular-level capillary, as represented by type (b) in Fig. 1.

3.3. Diffusion in molecular cavity

In order to confirm the explanation of the cavity structures obtained above, the diffusion behavior of noble gases, He, Ne, and Ar, was simulated. Because these gases do not plasticize polymers, the diffusion behavior directly reflects the structure and dynamics of the cavities. The diffusion process consists of vibrational motion in a cavity and jumping motion between cavities. The mean-square displacements (MSD) along each crystal axis were obtained through the long-time MD simulation. The diffusion coefficients of the gases along each crystal axis were calculated as

$$D = \lim_{t\to\infty} \frac{1}{2td} \langle |\mathbf{R}_i(t) - \mathbf{R}_i(0)|^2 \rangle, \tag{5}$$

where $\mathbf{R}_i(t)$ is the position vector of the *i*th gas molecule at time *t*, *d* the dimension, and $\langle \ldots \rangle$ means an ensemble average. The averaging is taken over 20 gas molecules and

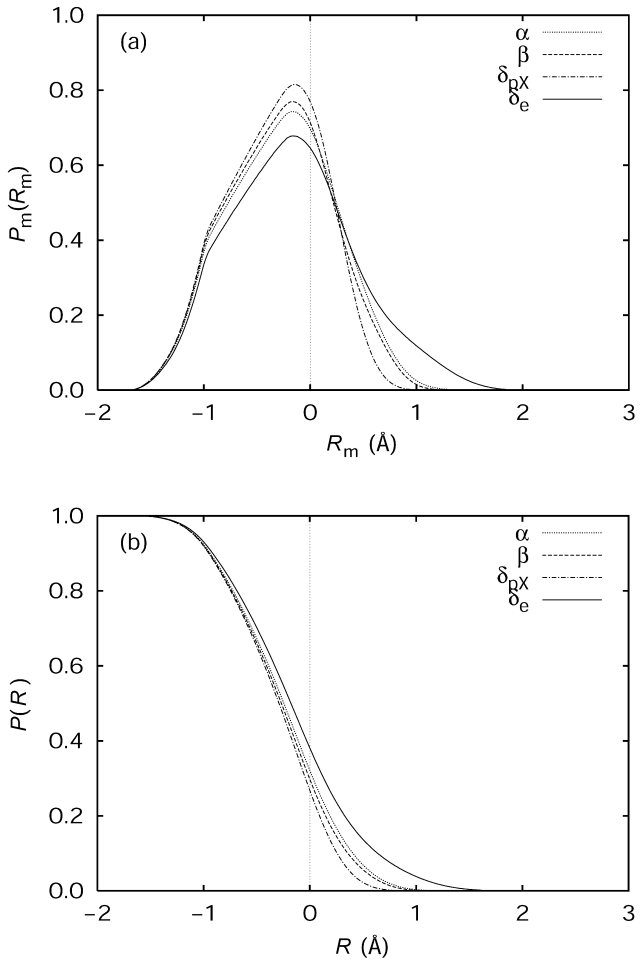

Fig. 3. Free volume distributions in the polymorphs of s-PS: (a) probability density of distance from the nearest atom surface in a unit cell, $P_m(R_m)$, and (b) ACV fraction, $P(R)$, as a function of probe radius R. The latter can be calculated from the former by Eq. (1).

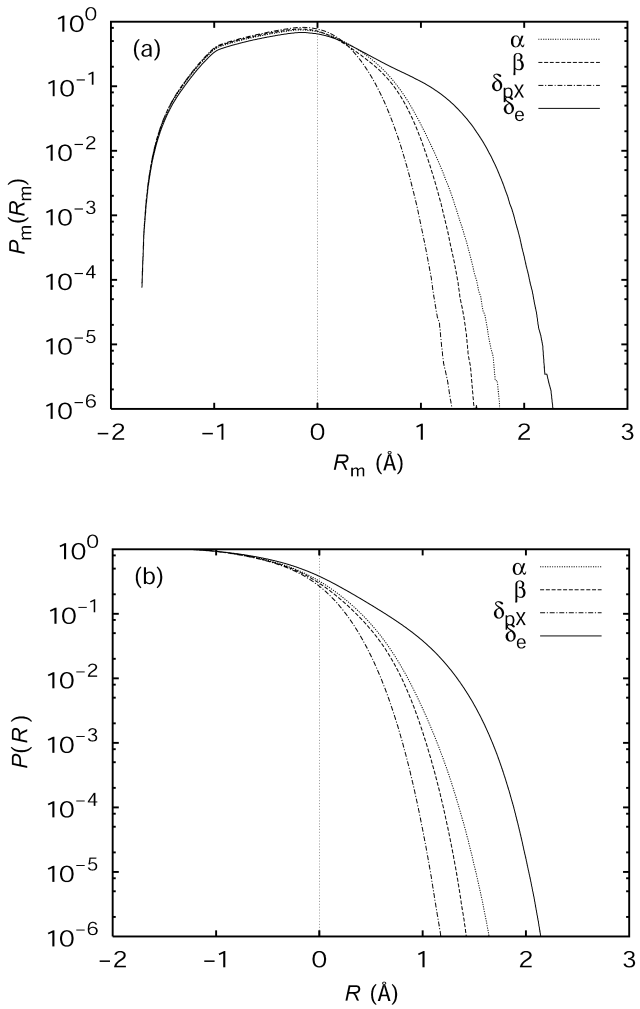

Fig. 4. Free volume distributions in the polymorphs of s-PS: the same functions as in Fig. 3 are plotted in a semi-logarithmic scale.

over all the possible time origins. The three-dimensional diffusion coefficient, D, and the one-dimensional ones along each crystal axis, D_a, D_b, and D_c, were calculated. The diffusion coefficients of the gases are listed in Tables 5–7, associated with anisotropy parameters.

In the α form (Table 5), the diffusion coefficients along the capillary (c-axis) are fairly large. The anisotropy of diffusion is enhanced for larger gases, Ne and Ar, whose diffusion behavior is almost governed by the one-dimensional transport. A simple diffusion model to describe the gas permeation behavior in semicrystalline s-PS was proposed by Hodge et al. [61], based on the gas transport

Table 5
Diffusion coefficients of noble gases along each crystal axis in α form at 300 K

Gas	D (cm^2/s)	D_a (cm^2/s)	D_b (cm^2/s)	D_c (cm^2/s)	$2D_c/(D_a+D_b)$
He	5.8×10^{-5}	4.6×10^{-5}	8.6×10^{-5}	6.5×10^{-5}	1.0
Ne	6.0×10^{-6}	0.0	0.0	1.8×10^{-5}	(∞)
Ar	1.2×10^{-6}	0.0	0.0	3.5×10^{-6}	(∞)

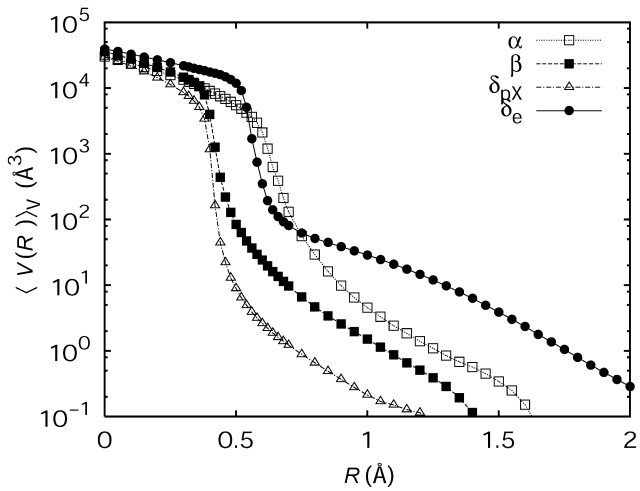

Fig. 5. Volume-weighted average of the volumes of individual accessible clusters, $\langle V(R)\rangle_V$, in the polymorphs of s-PS, as a function of the probe radius R.

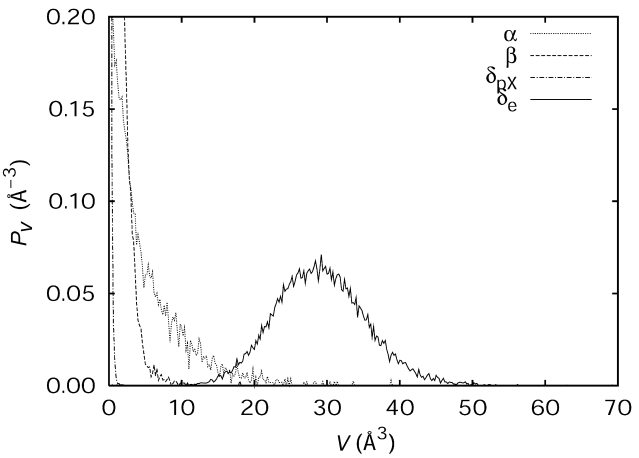

Fig. 6. Volume-weighted distribution of the volumes of individual accessible clusters for a probe of radius 1 Å.

measurements of oxygen and carbon dioxide in the α form. In the model, an anomalously higher mobility of gas molecules in the crystal than that in the amorphous phase was assumed; the assumption is based on the diffusion path along the crystal *c*-axis. The diffusion model of Hodge et al. [61] was clearly and directly substantiated by the simulation. The anisotropy of diffusion is, however, lost for the small gas, He.

In the β form (Table 6), the diffusion coefficients are approximately one order smaller than those in the α form. The diffusion paths are restricted in the $a-c$ plane; no jumping diffusion was observed along the *b*-axis even for He. The diffusion behavior is reasonable, considering the free volume structure shown in Fig. 2(b).

In the δ_e form (Table 7), no jumps between cavities are observed at 300 K except for He. The larger molecules

Table 6
Diffusion coefficients of noble gases along each crystal axis in β form at 300 K

Gas	D (cm^2/s)	D_a (cm^2/s)	D_b (cm^2/s)	D_c (cm^2/s)	D_a/D_c
He	1.0×10^{-5}	2.3×10^{-5}		8.3×10^{-6}	2.8
Ne	0.7×10^{-6}	1.4×10^{-6}		0.7×10^{-6}	2.0
Ar	0.2×10^{-6}	0.6×10^{-6}		0.2×10^{-6}	3.0

No jumping diffusion along *b*-axis was observed during simulation runs.

oscillate in each cavity throughout the simulation. The converged constant values of the root MSDs, which correspond to the amplitudes of oscillation, are shown in Table 8. That along the *c*-axis is much smaller than the others, reflecting the flat shape of the molecular cavity. At higher temperature, the narrow channels between the large cavities are occasionally opened even for the larger gas molecules to diffuse in the δ_e form because of the increase in mobility of the polymer chains.

The diffusion coefficients along the *c*-axis are smaller than those along the other directions. In the report of Milano et al. [42], the preferential diffusion pathways are parallel to the crystallographic $a-c$ plane. In our simulation, the diffusion in the $a-c$ plane were also observed. The diffusion path agrees reasonably with the connectivity of cavities, which are shown in the $a-c$ plane of Fig. 7(b). A hopping motion between cavities occurs along ⟨101⟩ directions. The jump distances of the gases are 8.7 and 3.9 Å for *a*- and *c*-axial directions, respectively, which can be estimated from the crystal periodicity (half values of the edge lengths *a* and *c*, respectively). Because the diffusion coefficients are proportional to the square of the jump distance, the expected ratio of D_a/D_c is 5.0. The ratio for the present simulation of

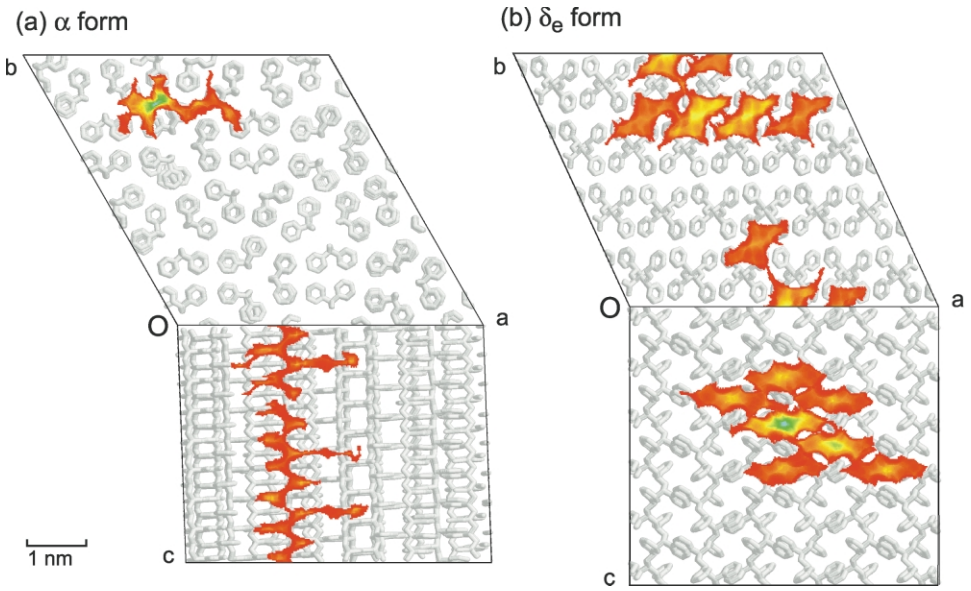

Fig. 7. Projections of one of the continuous accessible clusters in (a) α and (b) δ_e forms calculated for each critical probe radius, R_c, i.e. 0.7 and 0.6 Å, for α and δ_e forms, respectively. Note that there are many other accessible clusters in the unit cell. The cavities are superimposed on the snapshots of polymer chains. Only the carbon atoms are drawn for simplicity.

Table 7
Diffusion coefficients of noble gases along each crystal axis in δ_e form at 300, 400, and 500 K

Gas	D (cm^2/s)	D_a (cm^2/s)	D_b (cm^2/s)	D_c (cm^2/s)	D_a/D_c	D_b/D_c
$T = 300$ K						
He	5.2×10^{-6}	9.0×10^{-6}	6.8×10^{-6}	1.2×10^{-6}	7.5	5.7
Ne[a]						
Ar[a]						
$T = 400$ K						
He	3.9×10^{-5}	5.8×10^{-5}	6.0×10^{-5}	9.4×10^{-6}	6.2	6.4
Ne	1.4×10^{-6}	2.6×10^{-6}	1.5×10^{-6}	0.2×10^{-6}	13	7.5
Ar[b]	$<1 \times 10^{-7}$		$<1 \times 10^{-7}$			
$T = 500$ K						
He	1.2×10^{-4}	2.1×10^{-4}	1.4×10^{-4}	3.1×10^{-5}	6.8	4.5
Ne	1.1×10^{-5}	2.0×10^{-5}	1.4×10^{-5}	1.6×10^{-6}	13	8.8
Ar	0.5×10^{-6}	1.1×10^{-6}	0.4×10^{-6}	0.1×10^{-6}	11	4.0

[a] No jumping motion was observed during 5 ns.
[b] Only one jumping motion along b-axis was observed during 5 ns.

He is approximately 7, which is slightly higher than the expected value. The jump distance along the b-axis is estimated to be 11.73 Å, which is equal to the edge length b. Suppose the jump probability is the same between these two directions, the ratio of D_b/D_c becomes 9.0. The average value of $D_b/D_c = 5.5$ in the simulation implies the jump probability along the b-axis is 60% of that along the c-axis. This is because the diffusion along the b-axis requires the long-distance jump motion through the narrow channels, which are shown in the a–b plane of Fig. 7(b). Since the hopping motion along the b-axis is sometimes accompanied by that along the a-axis, the ratio of D_a/D_c becomes higher than 5.0, which is the expected value in the case that the diffusion is restricted on the a–c plane.

In the report of Milano et al. [42], the calculated diffusion coefficients of He at 298 K were $D_a = 7.9 \times 10^{-6}$, $D_{\perp ac} = 1.1 \times 10^{-6}$, and $D_c = 2.0 \times 10^{-6}$ cm^2/s. Since they used the quasi-orthorhombic unit cell, the value which is perpendicular to the a–c plane, $D_{\perp ac}$, was calculated instead of D_b. Although D_a and D_c values agree reasonably with our simulation, the value of $D_{\perp ac}$ is quite small. In their calculation, the length of the a-axis was 5% smaller than the experimental value because of the incorporation of the quasi-orthorhombic cell. This may lead to the narrowing of the diffusion channels along the b-axis and may result in the smaller value of $D_{\perp ac}$.

In the δ_e form, the diffusion coefficients remarkably depend on temperature. The ratio of the diffusion coefficients for gases of different sizes is quite large; D_{He}/D_{Ne} and D_{Ne}/D_{Ar} are in the range of 10–30. The δ_e form acts as a molecular sieve whose mesh size is controllable by changing the temperature. A detailed investigation on the diffusion mode will be presented in a forthcoming paper [62].

Table 8
Square root of plateau value of the mean-square displacement of noble gases along each crystal axis in δ_e form at 300 K (Å)

Gas	a-axis	b-axis	c-axis
Ne	3.47	2.66	0.87
Ar	2.48	2.16	0.60

3.4. Solubility in molecular cavity

The solubility of gases into the molecular cavity is also of much interest. The calculated solubilities of He, Ne, Ar, O_2, and CO_2 are plotted against their van der Waals radii in Fig. 8. The solubility is determined by two factors: the size and energy effects. It is difficult for the larger gases to dissolve in the β form because the cavity size is small for this form. On the other hand, the larger gases can easily dissolve in the δ_e form because the cavity size is large enough even for CO_2 molecules to occupy. The solubility of the larger gases becomes higher because the interaction with the host matrix is also large for these gases. In the α form, in which moderate size cavities exist, the two factors compensate each other; the solubilities are approximately constant for all the gases.

The experimental solubilities of O_2 and CO_2 in amorphous s-PS are 0.17 and 2.9 cm^3(STP)/cm^3 atm, respectively [61]. The values become lower in the α-form crystal; 0.09–0.11 and 1.8–2.3 cm^3(STP)/cm^3 atm, respectively, for a sample of crystallinity ~0.3 [61]. For the single crystals of crystallinity 1, which corresponds to the present simulation condition, lower solubilities are expected. Therefore, the simulation results are reasonable. For the crystals of low δ_e content, slightly higher solubilities than those in the amorphous s-PS were shown by the experiments [24]. The significantly higher solubilities calculated for the δ_e form are also reasonable because ideal limiting values for the single crystal can be obtained by the simulation.

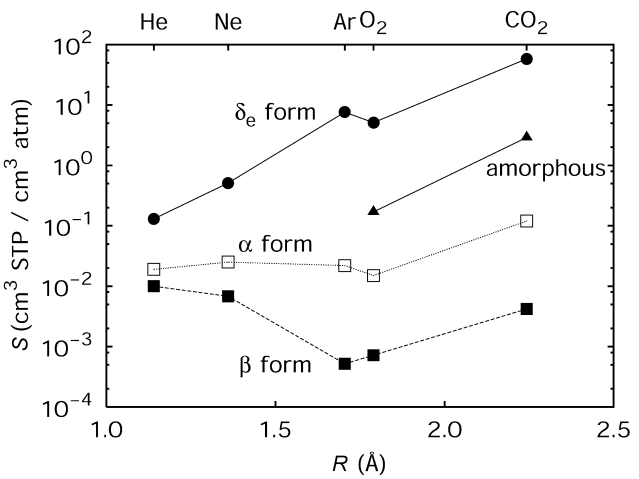

Fig. 8. Dependence of solubilities, S, on van der Waals radius. Open squares are the experimental values for amorphous s-PS [61]. The solubilities of the polyatomic molecules, O_2 and CO_2, are plotted against their effective van der Waals radii.

3.5. Application to 'smart membrane'

Smart membranes [1], which have precisely controlled molecular cavities, are expected to have significantly high permselectivity, which could be obtained neither by conventional rubbery, nor amorphous glassy, nor macroscopic porous membranes. The δ_e form may be used as the smart membrane, by which chemically alike molecules, such as *p*- and *m*-xylene, can be separated, utilizing the slight difference between the structure of the molecular cavity and that of guests [26]. Trace amounts of aromatic molecules may also be absorbed from contaminated water by the membrane. The fact that the larger gases show significantly high solubilities in the molecular cavity encourages the possibility of the strict separation of environmental hormones, which are large in size. Whether the substances really dissolve in the cavities is also determined by another factor, i.e. the diffusion paths in the crystals. The solubilities calculated by the present method are equilibrium ones. The diffusion processes in the δ_e form are governed by the narrow channels between the large cavities and are controllable by temperature, as presented above. Gases such as carbon dioxide and natural gas may be stored in the δ_e form, in combination with gating of permeation paths by pinpoint heating.

4. Conclusion

In summary, various nanoscale cavity structures in the polymorphs of crystalline s-PS were analyzed in detail. The cavity structure in the δ_e form can suitably be called a molecular cavity. The large individual holes with regular shape and size are connected in an orderly manner by the narrow channels. Another class of cavity structures, a kind of capillary, was found in the α form. The diffusion behavior and solubility of gases in the crystals were clearly interpreted in terms of the cavity structures. The hypothesis on the structure and connectivity of cavities derived from the present simulation is consistent with several experimental observations. The novel concept of the molecular cavity will be a breakthrough in the precise and effective separation of substances, e.g. carbon dioxide, hydrocarbons, and environmental hormones. Experimental studies on the sorption and diffusion of gases and aromatic molecules in the s-PS crystals are now in progress (Tsujita et al.), and results obtained so far corroborate those of our simulation.

Acknowledgements

The authors thank Prof. Y. Tsujita of the Nagoya Institute of Technology for the helpful discussions. This work is supported by a Grant-in-Aid for Scientific Research on Priority Areas (B) (No.13133203) from the Ministry of Education, Culture, Sports, Science and Technology, Japan.

References

[1] Tsujita Y. Unpublished.
[2] Sloan ED. Clathrate hydrate of natural gases. New York: Marcel-Dekker; 1990.
[3] Braga D. Chem Rev 1992;92:633–65.
[4] Nishikiori S, Kitazawa T, Kim CH, Iwamoto T. J Phys Chem A 2000; 104:2591–8.
[5] Meier WM, Olson DH, Baerlocher Ch, editors. Atlas of zeolite structure types, 4th ed. New York: Elsevier; 1996.
[6] Guerra G, Vitagliano VM, de Rosa C, Petraccone V, Corradini P. Macromolecules 1990;23:1539–44.
[7] Chatani Y, Shimane Y, Inoue Y, Inagaki T, Ishioka T, Ijitsu T, Yukinari T. Polymer 1992;33:488–92.
[8] Greis O, Xu Y, Asano T, Petermann J. Polymer 1989;30:590–4.
[9] De Rosa C, Guerra G, Petraccone V, Corradini P. Polym J 1991;23: 1435–42.
[10] De Rosa C. Macromolecules 1996;29:8460–5.
[11] Cartier L, Okihara T, Lotz B. Macromolecules 1998;31:3303–10.
[12] De Rosa C, Rapacciuolo M, Guerra G, Petraccone V, Corradini P. Polymer 1992;33:1423–8.
[13] Chatani Y, Shimane Y, Ijitsu T, Yukinari T. Polymer 1993;34: 1625–9.
[14] Chatani Y, Shimane Y, Inagaki T, Ijitsu T, Yukinari T, Shikuma H. Polymer 1993;34:1620–4.
[15] Chatani Y, Inagaki T, Shimane Y, Shikuma H. Polymer 1993;34: 4841–5.
[16] De Rosa C, Rizzo P, de Ballesteros OR, Petraccone V, Guerra G. Polymer 1999;40:2103–10.
[17] De Rosa C, Guerra G, Petraccone V, Pirozzi B. Macromolecules 1997;30:4147–52.
[18] Wang YK, Savage JD, Yang D, Hsu SL. Macromolecules 1992;25: 3659–66.
[19] Manfredi C, de Rosa C, Guerra G, Rapacciuolo M, Auriemma F, Corradini P. Macromol Chem Phys 1995;196:2795–808.
[20] Rizzo P, Lamberti M, Albunia AR, de Ballesteros OR, Guerra G. Macromolecules 2002;35:5854–60.
[21] Tamai Y, Fukuda M. Macromol Rapid Commun 2002;23:891–5.
[22] Manfredi C, del Nobile MA, Mensitieri G, Guerra G, Rapacciuolo M. J Polym Sci Polym Phys Ed 1997;35:133–40.
[23] Guerra G, Manfredi C, Musto P, Tavone S. Macromolecules 1998;31: 1329–34.
[24] Tsutsui K, Tsujita Y, Yoshimizu H, Kinoshita T. Polymer 1998;39: 5177–82.
[25] Guerra G, Milano G, Venditto V, Musto P, de Rosa C, Cavallo L. Chem Mater 2000;12:363–8.
[26] Sivakumar M, Yamamoto Y, Amutharani D, Tsujita Y, Yoshimizu H, Kinoshita T. Macromol Rapid Commun 2002;23:77–9.
[27] Shah VM, Stern SA, Ludovice PJ. Macromolecules 1989;22:4660–2.
[28] Rigby D, Roe RJ. Macromolecules 1990;23:5312–9.
[29] Arizzi S, Mott PH, Suter UW. J Polym Sci Polym Phys Ed 1992;30: 415–26.
[30] Greenfield ML, Theodorou DN. Macromolecules 1993;26:5461–72.
[31] Misra S, Mattice WL. Macromolecules 1993;26:7274–81.
[32] Tamai Y, Tanaka H, Nakanishi K. Macromolecules 1994;27: 4498–508.
[33] Tamai Y, Tanaka H, Nakanishi K. Macromolecules 1995;28: 2544–54.
[34] Lee S, Mattice WL. Comput Theor Polym Sci 1999;9:57–61.
[35] Doolittle AK. J Appl Phys 1951;22:1471–5.
[36] Doolittle AK. J Appl Phys 1952;23:236–9.
[37] Fox TG, Flory PJ. J Appl Phys 1950;21:581–91.
[38] Fox TG, Flory PJ. J Polym Sci 1954;14:315–9.
[39] Cohen MH, Turnbull D. J Chem Phys 1959;31:1164–9.
[40] Turnbull D, Cohen MH. J Chem Phys 1961;34:120–5.

[41] Milano G, Venditto V, Guerra G, Cavallo L, Ciambelli P, Sannino D. Chem Mater 2001;13:1506–11.
[42] Milano G, Guerra G, Müller-Plathe F. Chem Mater 2002;14:2977–82.
[43] Ryckaert JP, Ciccotti G, Berendsen HJC. J Comput Phys 1977;23:327–41.
[44] Cornell WD, Cieplak P, Bayly CI, Gould IR, Merz Jr DM, Ferguson KM, Spellmeyer DC, Fox T, Caldwell JW, Kollman PA. J Am Chem Soc 1995;117:5179–97.
[45] Smith GD, Ayyagari C, Jaffe RL, Pekny M, Bernarbo A. J Phys Chem A 1998;102:4694–702.
[46] Maitland GC, Rigby M, Smith EB, Wakeham WA. Intermolecular forces: their origin and determination. Oxford: Clarendon Press; 1981.
[47] Geiger LC, Ladanyi BM, Chapin ME. J Chem Phys 1990;93:4533–42.
[48] Fischer J, Lago S. J Chem Phys 1983;78:5750–8.
[49] Allen MP, Tildesley DJ. Computer simulation of liquids. Oxford: Oxford University Press; 1987.
[50] Nosé S. J Chem Phys 1984;81:511–9.
[51] Parrinello M, Rahman A. J Appl Phys 1981;52:7182–90.
[52] Verlet L. Phys Rev 1967;159:98–103.
[53] Ferrario M, Ryckaert JP. Mol Phys 1985;54:587–603.
[54] Pohorille A, Pratt LR. J Am Chem Soc 1990;112:5066–74.
[55] Pratt LR, Pohorille A. Proc Natl Acad Sci USA 1992;89:2995–9.
[56] Widom B. J Chem Phys 1963;39:2808–12.
[57] Deitrick GL, Scriven LE, Davis HT. J Chem Phys 1989;90:2370–85.
[58] Shing KS, Chung ST. J Phys Chem 1987;91:1674–81.
[59] Kusanagi H, Takase M, Chatani Y, Tadokoro H. J Polym Sci Polym Phys Ed 1978;16:131–42.
[60] Trezza E, Grassi A. Macromol Rapid Commun 2002;23:260–3.
[61] Hodge K, Prodpran T, Shenogina NB, Nazarenko S. J Polym Sci Polym Phys Ed 2001;39:2519–38.
[62] Tamai Y, Fukuda M. Manuscript in preparation.